frontiers in Earth Science

ORIGINAL RESEARCH
published: 21 May 2020
doi: 10.3389/feart.2020.00152

Experimental Evidence That Permafrost Thaw History and Mineral Composition Shape Abiotic Carbon Cycling in Thermokarst-Affected Stream Networks

Scott Zolkos† and Suzanne E. Tank*

Department of Biological Sciences, University of Alberta, Edmonton, AB, Canada

OPEN ACCESS

Edited by:
Katharine Rosemary Hendry, University of Bristol, United Kingdom

Reviewed by:
Aga Nowak, The University Centre in Svalbard, Norway
Francois L. L. Muller, National Sun Yat-sen University, Taiwan

***Correspondence:**
Scott Zolkos
sgzolkos@gmail.com

†Present address:
Scott Zolkos, Woods Hole Research Center, Falmouth, MA, United States

Specialty section:
This article was submitted to Geochemistry, a section of the journal Frontiers in Earth Science

Received: *22 February 2020*
Accepted: *22 April 2020*
Published: *21 May 2020*

Citation:
Zolkos S and Tank SE (2020) Experimental Evidence That Permafrost Thaw History and Mineral Composition Shape Abiotic Carbon Cycling in Thermokarst-Affected Stream Networks. Front. Earth Sci. 8:152. doi: 10.3389/feart.2020.00152

Mounting evidence suggests that biogeochemical processing of permafrost substrate will amplify dissolved inorganic carbon (DIC = $\Sigma[CO_2, HCO_3^-, CO_3^{2-}]$) production within Arctic freshwaters. The effects of permafrost thaw on DIC may be particularly strong where terrain subsidence following thaw (thermokarst) releases large amounts of sediment into fluvial networks. The mineral composition and chemical weathering of these sediments has critical yet untested implications for the degree to which streams represent a source of CO_2 to the atmosphere vs. a source of bicarbonate to downstream environments. Here, we experimentally determine the effects of mineral weathering on fluvial CO_2 by incubating sediments collected from three retrogressive thaw slump features on the Peel Plateau (NWT, Canada). Prehistoric warming and contemporary thermokarst have exposed sediments on the Peel Plateau to varying degrees of thaw and chemical weathering, allowing us to test the role of permafrost and substrate mineral composition on CO_2:HCO_3^- balance. We found that recently-thawed sediments (within years to decades) and previously un-thawed tills from deeper permafrost generated substantial amounts of solutes and DIC. These solutes and the mineralogy of sediments suggested that carbonate weathering coupled with sulfide oxidation was a net source of abiotic CO_2. Yet, on average, more than 30% of this CO_2 was converted to bicarbonate via carbonate buffering reactions. In contrast, the mineralogy and geochemical trends associated with sediments from the modern and paleo-active layer, which were exposed to thaw over longer timescales than deeper permafrost sediments, more strongly reflected silicate weathering. In treatments with sediment from the modern and paleo-active layer, minor carbonate and sulfide weathering resulted in some DIC and net CO_2 production. This CO_2 was not measurably diminished by carbonate buffering. Together, these trends suggest that prior exposure to thaw and weathering on the Peel Plateau reduced carbonate and sulfide in upper soil layers. We conclude that thermokarst unearthing deeper tills on the Peel Plateau will amplify regional inorganic carbon cycling

for decades to centuries. However, CO_2 consumption via carbonate buffering may partly counterbalance CO_2 production and release to the atmosphere. Regional variability in the mineral composition of permafrost, thaw history, and thermokarst intensity are among the primary controls on mineral weathering within permafrost carbon-climate feedbacks.

Keywords: carbonate, sulfide, carbon dioxide, thermokarst, retrogressive thaw slump

INTRODUCTION

Rapid climate warming and intensifying hydrologic cycles at northern latitudes (Serreze and Barry, 2011) are activating immense stores of organic carbon from perennially frozen permafrost soils into modern biogeochemical cycles (Biskaborn et al., 2019; Vonk et al., 2019). The biotic and abiotic processing of this relatively reactive carbon pool stands to amplify climate warming in the coming centuries by releasing large amounts of carbon dioxide (CO_2) from terrestrial and aquatic environments into Earth's atmosphere (Schuur et al., 2015; Turetsky et al., 2020). Along the terrestrial–freshwater continuum, carbonate equilibrium reactions drive the speciation of dissolved inorganic carbon ($DIC = \Sigma[CO_2, HCO_3^-, CO_3^{2-}]$) and therefore influence the susceptibility of carbon exchange with the atmosphere as CO_2 vs. export to downstream environments as carbonate alkalinity (HCO_3^-, CO_3^{2-}) (Stumm and Morgan, 1996). Changes to DIC cycling in northern permafrost-affected landscapes thus have potentially critical implications for carbon cycling and feedbacks to long-term climate, particularly where large amounts of permafrost substrate are mobilized directly into fluvial networks (Vonk et al., 2019).

Increasing fluxes of ions and carbonate alkalinity in major Arctic rivers in recent decades reflect enhanced DIC cycling coupled to a thickening of the seasonally-thawed active layer into more mineral-rich soil layers and accelerating physical erosion which exposes minerals to chemical weathering (Tank et al., 2016; Toohey et al., 2016; Drake et al., 2018b; Zolkos et al., 2018). Over geological timescales, the chemical weathering of these minerals may regulate climate by moderating atmospheric CO_2 (Berner, 1999; Maher and Chamberlain, 2014; Torres et al., 2014), while perturbation of these cycles can change contemporary carbon cycles (Gislason et al., 2009; Beaulieu et al., 2012). Carbonate and silicate weathering by carbonic acid [H_2CO_3*, including dissolved $CO_{2(g)}$] transforms atmospheric $CO_{2(g)}$ and biotic CO_2 produced by plant root respiration and microbial oxidation of soil organic matter into bicarbonate (HCO_3^-; Equations 1–3) (Berner, 1999), rendering it less susceptible to exchange with the atmosphere:

$$H_2O + CO_{2(g)} \rightleftharpoons H_2CO_3* \rightleftharpoons H^+ + HCO_3^- \rightleftharpoons 2H^+ + CO_3^{2-} \quad (1)$$

$$H_2CO_3* + (Ca, Mg)CO_3 \rightarrow (Ca^{2+}, Mg^{2+}) + 2HCO_3^- \quad (2)$$

$$2H_2CO_3* + 3H_2O + (Ca, Mg)Al_2Si_2O_8 \rightarrow (Ca^{2+}, Mg^{2+}) + 2HCO_3^- + 2Al_2Si_2O_5(OH)_4 \quad (3)$$

In contrast, sulfide oxidation (Equation 4) generates sulfuric acid (H_2SO_4) that either liberates mineral C into solution as H_2CO_3* (Equation 5) or HCO_3^- (Equation 6) via carbonate weathering, or generates no dissolved C via silicate weathering (Equation 7) (Lerman et al., 2007):

$$FeS_2 + 15/4O_2 + 7/2H_2O \rightarrow Fe(OH_3) + 2H_2SO_4 \quad (4)$$

$$2H_2SO_4 + 2(Ca, Mg)CO_3 \rightarrow 2(Ca^{2+}, Mg^{2+}) + 2SO_4^{2-} + 2H_2CO_3* \quad (5)$$

$$H_2SO_4 + 2(Ca, Mg)CO_3 \rightarrow 2(Ca^{2+}, Mg^{2+}) + SO_4^{2-} + 2HCO_3^- \quad (6)$$

$$H_2SO_4 + H_2O + (Ca, Mg)Al_2Si_2O_8 \rightarrow (Ca^{2+}, Mg^{2+}) + SO_4^{2-} + Al_2Si_2O_5(OH)_4 \quad (7)$$

When sediments are more limited in carbonates than in sulfides, H_2SO_4 from sulfide oxidation can lower pH and increase the CO_2 proportion of DIC (Equation 1), facilitating CO_2 release to the atmosphere (Stumm and Morgan, 1996). Half of the HCO_3^- transferred from streams and rivers into the marine carbon cycle returns to the atmosphere as CO_2 over geological timescales (Calmels et al., 2007). Thus, the balance between H_2CO_3 and H_2SO_4 weathering controls the degree to which mineral weathering is carbon neutral (Equation 2) vs. a carbon sink (Equation 3) or source (Equations 5, 6) (Calmels et al., 2007; Tank et al., 2012; Hindshaw et al., 2016) and acts as a positive or negative feedback to long-term climate warming (Berner, 1999; Gislason et al., 2009; Torres et al., 2014, 2017; Pogge von Strandmann et al., 2017). Constraining the sources of mineral weathering and the balance between CO_2 and HCO_3^- in northern fluvial networks can help to understand DIC cycling and the abiotic component of permafrost carbon-climate feedbacks.

Local and regional variation in lithology, physical erosion, and temperature are primary controls on the sources and magnitude of mineral weathering (Gaillardet et al., 1999; Li et al., 2017). For instance, riverine DIC can be relatively high in catchments with carbonate lithologies (Blum et al., 1998; Tank et al., 2012) as carbonates weather more readily than silicates (Stumm and Morgan, 1996). River chemistry reveals that physical erosion enhances solute production by exposing previously unweathered material (Riebe et al., 2001; West et al., 2005; Calmels et al., 2007) and by increasing the potential reactivity of sediments (Anderson, 2007). DIC cycling in terrains with glacial activity can be rapid. For instance, H_2CO_3* weathering of sediments during fluvial transport in pro-glacial streams can consume dissolved CO_2 to below atmospheric levels (St. Pierre et al., 2019). While much of Canada is no longer glaciated, terrain subsidence following permafrost thaw (thermokarst) across vast swaths of northwestern Canada is enabling large quantities of glaciogenic sediments that were emplaced by the former Laurentide Ice Sheet

to be mobilized into fluvial networks (Kokelj et al., 2017a). In these ice- and sediment-rich glacial margin landscapes like the Peel Plateau (NWT, Canada), retrogressive thaw slump (RTS) thermokarst activity can amplify DIC cycling and increase HCO_3^- in downstream environments (Zolkos et al., 2018). While H_2SO_4 carbonate weathering in thermokarst-affected streams on the Peel Plateau is thought to be a net source of CO_2 to the atmosphere over contemporary and longer timescales (Zolkos et al., 2018, 2019), the degree to which mineral weathering by H_2CO_3 consumes CO_2 in streams on the Peel Plateau remains untested. The balance between CO_2 and HCO_3^- in thermokarst-affected streams has important implications for the Arctic inorganic carbon cycle, as hillslope thermokarst features like RTSs may affect 900,000 km^2 (5%) of the northern permafrost region (Olefeldt et al., 2016). Further, the chemistries of streams on the Peel Plateau reflect weathering from sediment sources with varying degrees of prior exposure to thaw and thus mineral composition (Lacelle et al., 2019). Determining the influence of permafrost mineral composition and weathering sources on the balance between CO_2 and HCO_3^- in streams can thus help to understand thermokarst effects on DIC cycling and potential feedbacks to long-term climate.

Here, we refine understanding of mineral weathering contributions to inorganic carbon cycling on the Peel Plateau (NWT, Canada) (Zolkos et al., 2018), where accelerating thermokarst activity is mobilizing large volumes of mineral-rich glacial tills with varying degrees of prior thaw into fluvial networks (Kokelj et al., 2013; Segal et al., 2016a; van der Sluijs et al., 2018). We build on previous research that investigated the effects of RTSs on solutes, sediments, and organic carbon in fluvial networks (Kokelj et al., 2013; Malone et al., 2013; Littlefair et al., 2017), and Holocene environmental change on the composition of permafrost soil organic carbon and solution chemistry (Lacelle et al., 2019). To do this, we characterized the mineral composition of RTS sediments that commonly enter streams on the Peel Plateau and experimentally weathered these sediments to determine how thermokarst and thaw history affect DIC concentration and speciation (Segal et al., 2016a; Lacelle et al., 2019). Our results indicate that fluvial inorganic carbon cycling on the Peel Plateau is amplified by more intense thermokarst, which thaws deeper sediments containing a greater proportion of carbonate and sulfide. We conclude that thermokarst on the Peel Plateau and in similar Arctic environments may intensify inorganic carbon cycling in fluvial networks for centuries.

MATERIALS AND METHODS

Study Area and Retrogressive Thaw Slump Sites

The Peel Plateau is characterized by permafrost tills up to 50 m in thickness underlain by sandstone and siltstone bedrock (Norris, 1985; Kokelj et al., 2017b). These tills are mainly comprised of carbonates, sulfides, silicates, and gypsum (Malone et al., 2013; Zolkos et al., 2018) likely derived from regional carbonate and shale bedrock (Norris, 1985; Stott, 1991) that was integrated into the Laurentide Ice Sheet (LIS) during its westward expansion. The last glacial maximum in the Peel Plateau region at around 18,500 cal yr BP (Lacelle et al., 2013) was followed by retreat of the LIS and early Holocene warming at 12,000–8,500 cal yr BP (Kokelj et al., 2017b). This warming promoted thaw of the ground surface, mineral weathering, and the accumulation of organic matter in the upper few meters of soil (Burn, 1997; Lacelle, 2004; Malone et al., 2013). A cooling climate 7,000–5,500 cal yr BP supported permafrost aggradation and the preservation of this solute- and organic-rich Holocene layer above the deeper, ice-rich Pleistocene sediments that have been isolated from thaw and exposure (Lacelle et al., 2013; Kokelj et al., 2017b). The shallow Holocene and the deeper Pleistocene permafrost layers are geochemically distinct and distinguished stratigraphically by an undulating thaw unconformity typically encountered 1.5–3 m below the surface (Malone et al., 2013) (**Figure 1A**).

The modern-day Peel Plateau is within the continuous permafrost zone and is comprised of ice-rich hummocky moraine, glaciofluvial, glaciolacustrine, and colluvial deposits (Duk-Rodkin and Hughes, 1992). Incised valleys and sloping terrain host hundreds of RTSs (**Figure 1**) (Kokelj et al., 2013; Lacelle et al., 2015; Segal et al., 2016a). The upslope growth of RTS features is sustained by the ablation of a vertical permafrost headwall of exposed ground ice and the downslope evacuation of a thawed slurry of slumped materials via fluidized flows which are enhanced by rainfall (Kokelj et al., 2015) (**Figure 1A**). Meltwater from the thawing headwall and its interaction with thawing substrate produce sediment- and solute-rich runoff often conveyed through rill channels in the scar zone (henceforth "runoff"), and into streams. The thawed materials that flow from thawing slopes are deposited as debris tongues that can grow over time to reach >1 km in length and tens of meters in thickness (van der Sluijs et al., 2018). These features are reshaped by the addition of debris from thawing slopes and erosion by the adjacent streams (Kokelj et al., 2015) (**Figure 1B**). Sediments unearthed by RTSs can be broadly categorized into five sources of material with varying degrees of prior exposure to thaw and weathering: (i) the seasonally-thawed *active layer*; (ii) the relatively organic- and solute-rich paleo-active layer contained in *Holocene-aged permafrost*; (iii) the un-thawed *Pleistocene-aged permafrost* sediments derived from glacial tills; and the composite of these three components, that are either recently mobilized and are undergoing active transport as fluvial suspended sediment in *runoff* (iv) or deposited in recent years to decades within the *debris tongue* (v) (**Figure 1**). Active layer and Holocene permafrost sediments in RTSs on the Peel Plateau have been exposed to thaw for decades to centuries, whereas Pleistocene permafrost sediments were frozen upon their deposition and have remained sequestered within permafrost for millennia.

The three focal RTSs in this study are situated within the ~1,100 km^2 Stony Creek watershed, west of Fort McPherson, NWT (**Figure 1**, **Table 1**). The RTS FM2 is among the largest active RTS features on the Peel Plateau (Lacelle et al., 2015) and has persisted for at least 70 years (Kokelj et al., 2015; van der Sluijs et al., 2018). The RTS HC is moderately-sized and estimates from the field suggest it is likely at least several decades old. The RTS HD scar zone was <1 ha at the time of sampling and visual

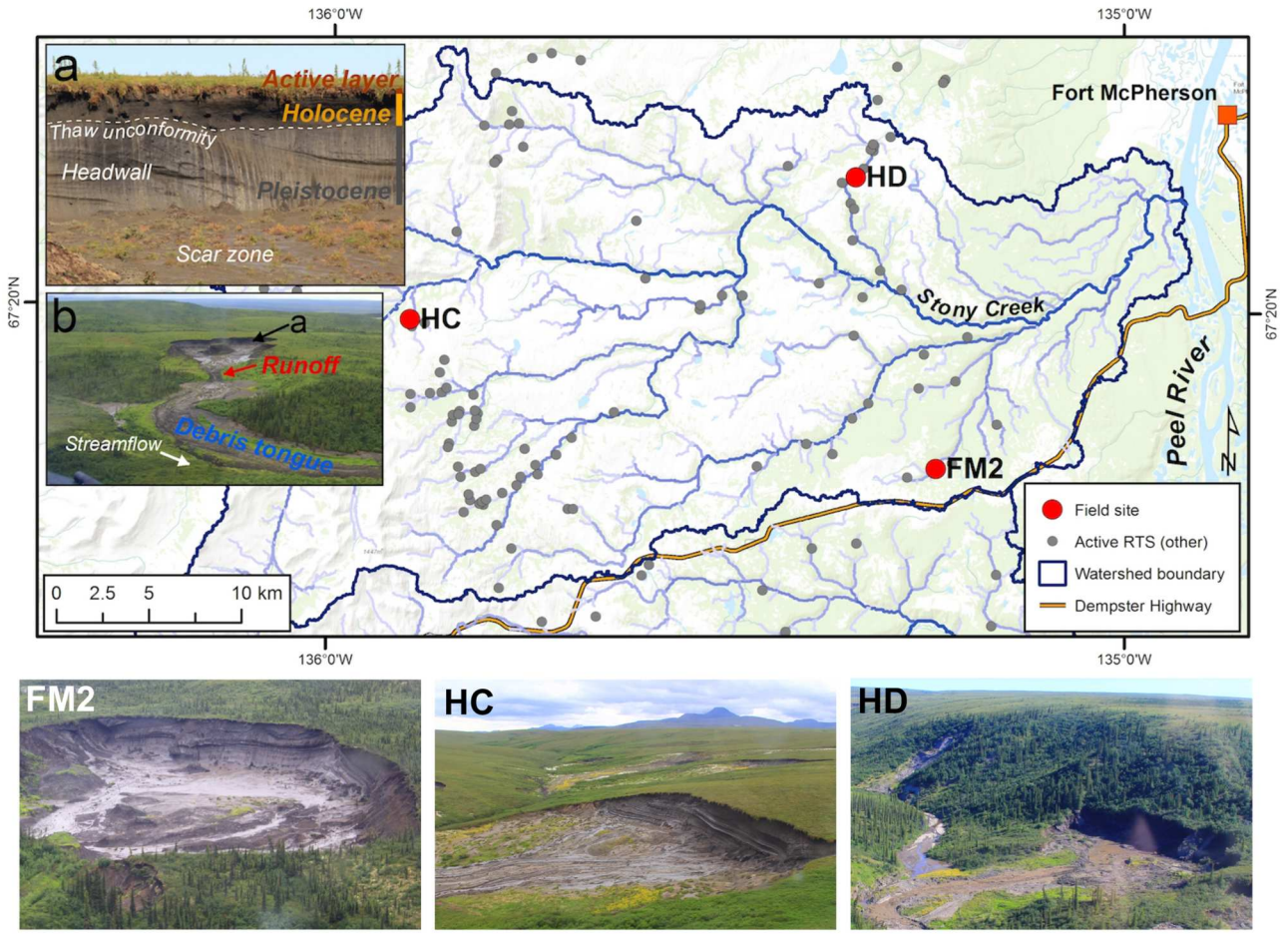

FIGURE 1 | Map of retrogressive thaw slump (RTS) study sites ($n = 3$) on the Peel Plateau (NWT, Canada) from which sediments for the experiment were collected. Sediments were collected from RTS FM2, HC, and HD (see photos below and locations on map). Photos were taken in 2014 (FM2) and 2017 (HC, HD). The photo of FM2 captures its southern lobe only. Insets (a) and (b) depict sampling locations of the five sediment sources (i.e., treatments) detailed in the text. Note location of inset (a) shown in (b). Inset photos depict sediment sources common to all RTS that were sampled for the experiment (RTS in inset photos from this region but not study). Basemap from Esri ArcGIS Online; "Active RTS" points on map from Segal et al. (2016b).

observations of Landsat 5 satellite imagery suggest that it formed circa 1998–2000.

Field sampling

During summer 2017, we collected active layer and permafrost sediments from the vertical headwall exposure, in addition to runoff and debris tongue sediments at RTS features FM2, HC, and HD (**Figure 1**, **Table 1**). These three RTS features were selected to capture potential variability in sediment geochemistry associated with varying compositions of glaciogenic materials (Duk-Rodkin and Hughes, 1992). To characterize RTS morphology, we measured headwall height at the time of sampling using a Uineye HK1200 laser range finder (±30 cm/0.35° accuracy) (Zolkos and Tank, 2019). Holocene and Pleistocene permafrost samples were collected in each RTS feature using a mallet and stainless-steel chisel. Permafrost layers were differentiated in the field based on cryostratigraphy (Lacelle et al., 2013) and later in the laboratory using stable isotopes of water ($\delta^{18}O$), to ensure isotopic values reflected previously published values for Holocene ($\delta^{18}O = -17$ to 25‰) and Pleistocene ($\delta^{18}O = -26$ to -32‰) ground-ice (Michel, 2011; Fritz et al., 2012; Lacelle et al., 2013). Active layer and debris tongue samples were collected using a stainless-steel trowel. Active layer material was composited from two roughly equal plugs of material from the A and B horizons (below the organic layer and above permafrost table). Debris tongue samples comprised of thawed, colluviated materials were collected near the adjacent stream, distant from the active headwall, reflecting sediments that have been thawed for years to decades. For active layer, permafrost, and debris tongue samples, the outer 5–10 cm of material was removed and discarded prior to sampling. Samples were stored in 5 L Whirlpak bags. Runoff was collected in pre-cleaned, triple-sample-rinsed 2 L HDPE bottles and stored chilled (4°C). Permafrost was thawed, and thawed permafrost and runoff were allowed to settle in the laboratory for 24 h at 4°C. Prior to drying sediments at

TABLE 1 | Characteristics of RTS features in this study.

RTS	Lat (DD)	Lon (DD)	$\delta^{18}O$ Holocene	$\delta^{18}O$ Pleistocene	Height (m, max)	Debris tongue length (~m)*	Scar zone (~ha)*
FM2	67.257	−135.236	−20.3	−28.3	24.2	1,600	27
HC	67.328	−135.900	−21.6	−29.2	18.3	180	2.5
HD	67.400	−135.334	−21.8	−30.3	13.6	150	0.6

*All headwall height measurements were made during July 2017. Stable water isotope ($\delta^{18}O$) values are reported in ‰ Vienna Standard Mean Ocean Water. *Estimated from satellite imagery and/or field photos; excludes area of debris tongue.*

20°C, supernatant was removed to limit the precipitation of secondary minerals.

Sediment Mineralogy and Geochemistry

Prior to mineral analysis by X-ray diffraction (XRD), dried sediments were gently disaggregated with a mallet, sieved to <250 μm, and visible organic matter was removed. Samples were not pretreated prior to analysis and XRD spectra were visually inspected to confirm minimal interference from organic matter (Mandile and Hutton, 1995). Sieved sediments were then finely ground with a ceramic mortar and pestle, and mineralogy was analyzed at the University of Alberta by XRD (Rigaku Ultimate IV), using Cobalt radiation at 0.6 s/step and 0.02° steps (detection limit = 3%). The geochemical composition of sediments was analyzed by inductively coupled plasma mass spectrometer (Perkin Elmer Elan 6000 Quadrupole ICP-MS) at the University of Alberta Canadian Center for Isotope Microanalysis, following Cooper et al. (2008). The coefficient of variation for Al^{3+}, Fe^{2+}, K^+, Mg^{2+}, Ca^{2+}, Na^+, and Sr^{2+} is <6%. Subsamples (0.2 ± 0.02 g) of the sieved sediments were dissolved via sequential digestions using HF + HNO_3^- and then HCl + HNO_3^-. Sediments were mixed with five mL of each acid (trace metal-grade), heated to 130°C, and digested overnight until dry. Finally, 10 mL 8N HNO_3^- were added, heated to 130°C, and a 1 mL aliquot was mixed with 0.1 mL HNO_3^-, 0.1 mL of internal standards (In, Bi, and Sc), and 8.8 mL of MilliQ deionized water.

Mineral Weathering Experiment

To determine how varying degrees of prior thaw and biogeochemical alteration of glaciogenic materials can influence DIC cycling on the Peel Plateau, we incubated active layer, Holocene, Pleistocene, runoff, and debris tongue sediments under controlled conditions. Following collection and sieving (see above), unground sediments were sterilized in precombusted aluminum trays at 200°C for 24 h in a forced-draft oven (Wolf and Skipper, 1994) to isolate the abiotic controls on DIC speciation from CO_2 production by microbial oxidation of organic matter. In our experiment this likely inhibited microbial sulfide oxidation (Singer and Stumm, 1970), which is a primary biotic mechanism of carbonate and silicate weathering in glaciated environments (Montross et al., 2013; Tranter and Wadham, 2014; Hindshaw et al., 2016), thus constraining possible sulfide oxidation to abiotic pathways involving Fe^{3+} (Rimstidt and Vaughan, 2003) and dissolved O_2 (Calmels et al., 2007). Sterilization was tested by mixing sterile MilliQ water (0.2 μm-filtered, ultraviolet light-treated) with the sterilized sediment, and extracting and incubating the supernatant on nutrient-rich agar plates (37°C, 7 d; Zuberer, 1994). Sterilization was confirmed by no observable growth compared to identical sediments that had not been sterilized. To evaluate the relative importance of sulfide oxidation and gypsum dissolution to SO_4^{2-} production, we assumed that 1 mol O_2 could yield 0.53 mol H_2SO_4 via sulfide oxidation (Equation 4) and we calculated the concentration of dissolved O_2 in the bottles under equilibrium conditions (10°C) to be 348 μM. This approach allowed us to estimate that SO_4^{2-} concentrations up to 184 μM could originate from sulfide oxidation via the dissolved O_2 pathway (Equations 5, 6). We interpreted higher SO_4^{2-} concentrations and the absence of sulfides from XRD detection as indicators of relatively greater SO_4^{2-} production from gypsum dissolution.

Sterilized sediments were incubated at total suspended solid concentrations (1,800 mg L^{-1}) and water temperatures (10°C) representative of stream reaches immediately downstream of RTS features during the 2015 sampling season (Zolkos et al., 2018). We inoculated 200 mL of MilliQ water with 3.6 g of sterilized sediment in acid-washed, precombusted (5 h, 500°C) 250 mL glass bottles and sealed them with two silicone-teflon septa (Skidmore et al., 2004). For each sediment source, 12 identical bottles were prepared and replicate bottles were terminated at 0.17, 1, 6, 24, 72, and 168 h. Two control bottles containing only MilliQ water were also terminated at 168 h. We enabled weathering to proceed under closed system conditions by flushing headspace in bottles with N_2 gas, enabling dissolved CO_2 and O_2 to contribute to carbonate weathering and sulfide oxidation. For RTS HD runoff, we had only enough sediment to run replicate bottles that were terminated at 168 h and we had no replicates for the other time points. To induce sediment suspension, all bottles were incubated on a rotary shaker set to 250 rpm during the course of the experiment, following Skidmore et al. (2004).

Chemical Analyses

At each time point, bottles were removed and water was filtered (0.45-μm, polyethersulfone, ThermoScientific) for DIC, pH, and conductivity measurements. Water was also equilibrated with nitrogen gas to extract dissolved gas for measurements of CO_2 concentration and stable carbon isotope analysis of CO_2 ($\delta^{13}C_{CO_2}$) (see below). Filtrate for DIC was stored without headspace in precombusted 12 mL exetainers, sealed with butyl septa, and refrigerated until analysis within 2 weeks (Apollo SciTech DIC analyzer). DIC standard curves were

built from certified reference material (Scripps Institution of Oceanography) and, when required for low-DIC samples, from 100 or 600 μM solutions prepared from a 1,000 ppm Na_2CO_3-$NaHCO_3$ DIC standard (ACCUSPEC). pH and conductivity were analyzed within 2 h of filtering. pH was analyzed with a Mettler Toledo FiveEasy benchtop meter calibrated daily using a two-point calibration curve (7.01 and 10.01 pH, NIST). The mean pH of replicate samples was calculated by first converting pH to H^+. Conductivity was analyzed with a Thermo Orion 115 A+ meter calibrated daily using 1,413 μS cm^{-1} solution. Dissolved CO_2 was extracted by equilibrating 20 mL of sample with 40 mL of nitrogen gas in an air-tight polypropylene syringe (Hesslein et al., 1991) and measured immediately by infrared gas analyzer (IRGA; PP Systems EGM-4). IRGA drift was checked daily with 60 mL of 1,010 ppm CO_2 standard (Scotty Gases). CO_2 concentration (μM) and the partial pressure of CO_2 (pCO_2) were calculated using Henry's constants corrected for water temperature (Weiss, 1974). For instances when DIC concentration could not be measured by the Apollo, DIC concentration was calculated using pH and pCO_2 as inputs to CO_2sys (v.2.3; Pierrot et al., 2006).

At the final time point of each experiment, water was also filtered (0.45-μm, cellulose acetate, Sartorius) to determine the concentrations of cations and anions. Cations were preserved with trace metal-grade HNO_3 and all ions were refrigerated until analysis at the University of Alberta Biogeochemical Analytical Services Laboratory (BASL, ISO/EIC 17025) following standard procedures. Equilibrated headspace gas samples for $\delta^{13}C_{CO_2}$ were stored over-pressurized in bottles that were sealed with baked (12 h, 60°C) butyl stoppers and pre-evacuated. $\delta^{13}C_{CO_2}$ was analyzed within 2 months by a Picarro isotope analyzer (G2201-*I*; < 0.2‰ precision) equipped with an injection module for discrete samples (SSIM). The Picarro analyzer was checked for drift against commercial and in-house $\delta^{13}C_{CO_2}$ standards during each run.

$\delta^{18}O$ of permafrost ice was analyzed by cavity ringdown spectroscopy (Picarro L2130-i) at the University of Alberta BASL. Calibration curves for water isotopes were built from U.S. Geological Survey secondary standards (USGS45 and USGS46) and in-house tap water, and calibrated by an International Atomic Energy Agency standard as a quality control.

Data Analysis

We report treatment replicates as mean ± standard deviation for DIC, CO_2, and conductivity and mean ± range for pH. We used the proportions of solute equivalent concentrations in a Piper diagram (Piper, 1944) to characterize potential mineral weathering reactions (see also Lehn et al., 2017). Calculations were made using the concentrations of cations and anions in the experiment bottles at 168 h, first correcting for the solute concentrations measured in the MilliQ control bottles (**Table A1** and **Supplementary Material**). For the Piper diagram, we calculated HCO_3^- as $\Sigma[HCO_3^-, CO_2]$, to correct for HCO_3^- hydrolysis to CO_2. The concentrations of dissolved CO_2 measured at each time point were corrected for dissolved atmospheric CO_2 in the control bottles (15–26 μM). To test for multivariate similarity (i.e., geochemical likeness) between treatments, we first performed a hierarchical cluster analysis using the R software package *pvclust* (Suzuki and Shimodaira, 2015), which employs the R base function *hclust* to generate a bootstrapped (n = 1,000 iterations), Euclidean distance-based estimate of a stable configuration of measurement clusters. Variables were selected for the *pvclust* to yield insight about DIC concentration and speciation (HCO_3^-, CO_2) and CO_2 source ($\delta^{13}C_{CO_2}$); to help differentiate between silicate and carbonate weathering (Al^{3+}); and to evaluate contributions from sulfide oxidation and gypsum dissolution (SO_4^{2-}). We then evaluated the associations between these geochemical variables and the sample clusters defined by *pvclust* using the *metaMDS* function in the R software package *vegan* (Oksanen et al., 2013). *metaMDS* augments traditional non-metric multidimensional scaling (NMDS) by running multiple MDS iterations to find a stable solution, whereby proximity of measurements indicates similarity and vectors reveal how variables correlate with measurements. All statistics were performed in R software v.3.4.4 (R Core Team, 2018), with significance interpreted at $\alpha = 0.05$.

RESULTS

Sediment Mineral and Geochemical Composition

Permafrost sediments, RTS runoff, and debris tongue deposits contained carbonates (calcite, dolomite, and rarely siderite), pyrite, gypsum, quartz, and various Na-, Mg-, and K-aluminosilicates (**Table 2**; note the XRD detection limit of 3%). Albite, clinochlore, muscovite, and quartz were detected in all sediment sources. The XRD detected carbonates, pyrite, and gypsum in at least half of the sediment sources and in at least one source at each RTS. Carbonates, sulfides, and gypsum were generally present (>3%) in Pleistocene permafrost sediments and absent from active layer sediments (below detection), whereas the presence of these minerals in Holocene, runoff, and debris tongue sediments varied (**Table 2**). The presence of sulfide and/or carbonate varied among sediment sources, and there were no sediments where carbonate was detected by XRD and sulfide was not.

The geochemical composition of sediments was characterized by—in decreasing order of concentration—Al^{3+}, Fe^{2+}, K^+, Mg^{2+}, Ca^{2+}, Na^+, and Sr^{2+} (**Table 3**). Because concentrations of Ca^{2+} relative to Na^+ and Sr^{2+} are typically higher for carbonates than silicates (Keller et al., 2007), we used molar ratios to discern the relative proportion of carbonates (high Ca/Na and Ca/Sr) vs. silicates in sediments. Ca/Sr and Ca/Na were typically higher in sediments where carbonates were detected by XRD (**Table 2**, **Figure 2**). Some sediments with sulfides but not carbonates also had relatively high Ca/Na and Ca/Sr (e.g., FM2 Holocene and Pleistocene, HD debris tongue), perhaps reflecting the presence of carbonates below the XRD detection limit.

Weathering Experiment: Trends in Conductivity, DIC, CO_2, and pH

For all RTSs and sediment sources, conductivity increased most strongly during the first 10 min of the incubation, and increased marginally thereafter, indicating that the

TABLE 2 | Minerals detected by X-ray diffraction (x) in non-sterilized sediments.

RTS	Source	Cluster	Gypsum $CaSO_4 \cdot 2H_2O$	Pyrite FeS_2	Calcite $CaCO_3$	Dolomite $CaMg(CO_3)_2$	Albite $Na(AlSi_3O_8)$	Orthoclase/sanidine $K(AlSi_3O_8)$	Clinochlore $Mg_5Al(AlSiO_{10})(OH)_8$	Muscovite $KAl_2(AlSi_3O_{10})(OH)_2$	Quartz SiO_2	Other
FM2	AL	3							X	x	x	
FM2	HO	3		X					X	x	x	
FM2	PL	2	x	X			x	x	X	x	x	
FM2	RU	1	x	X	x	x	x	x	X	x	x	
FM2	DT	1	x	X	x	x	x	x	x	x	x	
HC	AL	3							x	x	x	
HC	HO	1	x	X		x	x	x	x	x	x	
HC	PL	1		X	x	x	x	x	x	x	x	
HC	RU	1		X		x	x	x	x	x	x	*
HC	DT	1	x	x		x	x	x	x	x	x	
HD	AL	3							x	x	x	
HD	HO	3							x	x	x	
HD	PL	1	x	x	x	x	x		x	x	x	
HD	RU	2							x	x	x	†
HD	DT	2	x	x			x	x	x	x	x	

*AL, active layer; HO, Holocene; PL, Pleistocene; RU, runoff; DT, debris tongue. Other minerals: *Siderite: $FeCO_3$; † Lepidolite: $KLi_2Al(Si_4O_{10})(F,OH)_2$.*

TABLE 3 | Geochemical composition of sediments, measured by ICP-MS. Concentrations are reported in μmol g^{-1} of dry sediment.

Site	Source	Cluster	Al^{3+}	Fe^{2+}	K^+	Mg^{2+}	Ca^{2+}	Na^+	Sr^{2+}
FM2	AL	3	1,665	650	435	319	159	218	1.15
FM2	HO*	3	1,454	635	376	291	234	194	1.21
FM2	PL*	2	2,458	684	665	480	153	152	1.60
FM2	RU**	1	1,584	627	420	395	271	246	1.31
FM2	DT**	1	1,601	629	467	388	256	208	1.34
HC	AL	3	1,811	599	454	302	53	206	1.08
HC	HO**	1	1,722	594	495	396	240	207	1.26
HC	PL**	1	1,324	526	341	284	188	201	1.17
HC	RU**	1	1,560	556	430	359	175	237	1.32
HC	DT**	1	1,586	593	441	371	169	246	1.24
HD	AL	3	1,625	600	494	302	31	198	1.15
HD	HO	3	2,010	605	511	336	49	196	1.37
HD	PL**	1	1,986	646	519	402	202	195	1.38
HD	RU	2	2,330	752	651	479	113	181	1.51
HD	DT*	2	1,799	649	506	380	142	208	1.36

*Minerals detected by XRD: **Sulfides and carbonates, *sulfides.*

majority of the most reactive component of the mineral pool weathered by 168 h (**Figures 3A–C**). At 168 h, conductivity in treatments with Pleistocene permafrost, runoff, and debris tongue sediments (mean = 264 μS cm^{-1}) was significantly higher than in treatments with active layer and Holocene permafrost sediments [mean = 138 μS cm^{-1}, excluding HC Holocene [552 μS cm^{-1}]] (*t*-test: $t_{18} = 3.26$, $p < 0.001$). Solutes at 168 h broadly reflected sulfide oxidation and sulfate salt (e.g., gypsum) dissolution (SSD) and relatively greater contributions from silicate and carbonate weathering by H_2SO_4 than H_2CO_3 (**Figure 4**). Across RTSs and sediment sources, SO_4^{2-} concentrations at 168 h were often greater than would be expected from sulfide oxidation alone (section Mineral Weathering Experiment) (**Table 4**), suggesting that gypsum dissolution was a primary source of SO_4^{2-} in our experiment.

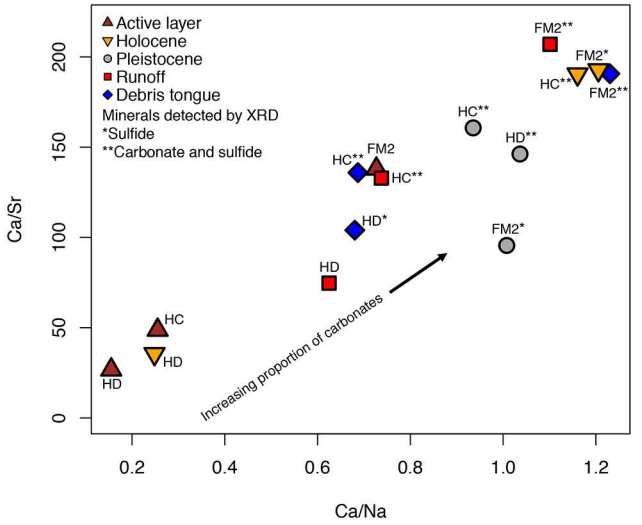

FIGURE 2 | The relationship between Ca/Sr (μmol g^{-1}/μmol g^{-1}) and Ca/Na (μmol g^{-1}/μmol g^{-1}) of sediments used in the mineral weathering experiment.

For all treatments, DIC concentrations increased rapidly during the first 6 h and more gradually after 24–48 h. Treatments containing sediments with carbonates and sulfides detected by XRD generated more DIC (mean = 728 μM after 168 h) than those in which only sulfides were detected (mean = 345 μM), or neither carbonates nor sulfides were detected (mean = 121 μM) (**Figures 3D–F**, **Table 4**). Accordingly, treatments with active layer and Holocene sediments generally had the lowest DIC at 168 h (mean = 111 and 342 μM, respectively), whereas DIC in treatments with Pleistocene, runoff, and debris tongue sediments had higher concentrations (581, 556, and 654 μM, respectively) (**Table 4**).

For all treatments, CO_2 increased rapidly within 6 h (**Figures 3G–I**) and, in treatments containing sediments with both carbonates and sulfides detected by XRD, decreased by 16–39 μM thereafter. The decrease in CO_2 was equivalent to 19–51% (mean = 33%) of the maximum CO_2 reached during the experiment for these treatments. At 168 h, CO_2 in these treatments was lower (mean = 75 μM) than in other treatments. In contrast, CO_2 in treatments containing sediments with sulfides but not carbonates detected by XRD generally reached the highest concentrations of CO_2 by 168 h (mean = 212 μM). Most of the treatments with active layer and Holocene sediments, which did not have carbonates or sulfides detected by XRD, had variable but relatively moderate CO_2 (mean = 95 μM).

pH increased in all treatments except for those with FM2 active layer sediments, which decreased from 7.04 to 6.69 pH units after 24 h. By 168 h, pH was highest where carbonates and sulfides were detected by XRD (mean = 7.23 pH units), lower when sulfides but not carbonates were detected (mean = 6.62), and the lowest in treatments where neither carbonates nor sulfides were detected (mean = 4.70) (**Figures 3J–L**).

Statistical Clusters of Treatments Based on Geochemistry

The cluster analysis revealed that treatments grouped into three geochemical clusters which broadly reflected gradients of prior thaw and exposure to weathering, and also the intensity of sulfide oxidation relative to carbonate weathering (**Figure A1**). Clusters one and two mostly included samples with more limited prior thaw compared to cluster three, which contained most of the active layer and Holocene permafrost sediments (**Figure 5**). Cluster one included sediments characterized by carbonate weathering that buffered H_2SO_4 acidity from sulfide oxidation more effectively than the sediments in cluster two. Cluster three included sediments which had relatively limited effects on DIC upon weathering. These statistical clusters help to describe the influence of prior exposure to thaw and the balance between carbonate weathering and sulfide oxidation on the evolution of DIC and CO_2 during the experiment.

Cluster 1—High DIC and pH, Low Al^{3+}

Treatments containing sediments with both carbonates and sulfides detected by XRD (**Table 2**) had consistently high DIC (mean = 728 μM), elevated pH (mean = 7.22 pH units), and low dissolved Al^{3+} (mean = 0.1 μM) (**Figure 3**, **Table 4**). In this cluster, mineral weathering resulted in rapid CO_2 production early in the experiment followed by a decrease after ~24 h. Yet, CO_2 was always higher than in the control bottles. $\delta^{13}C_{CO_2}$ at 168 h varied between treatments, but was generally intermediate (−8.3 to −13.2‰, n = 7) relative to samples in the other clusters (**Table 4**). Treatments in this cluster include Pleistocene permafrost sediments or recently thawed/colluviated material (i.e., runoff or debris tongue sediments), but not sediments from the active layer or Holocene permafrost.

Cluster 2—High SO_4^{2-} and CO_2, ^{13}C-Enriched CO_2

Bottles with FM2 Pleistocene, HD runoff, and HD debris tongue sediments had the highest CO_2 concentrations (**Table 4**), with no measurable decrease in CO_2 during the 168 h incubation. Generally, these treatments had ^{13}C-enriched CO_2 (−4.7 to −7.8‰), high concentrations of SO_4^{2-} (mean = 1,307 μM), and had sulfides and gypsum detected by XRD (except for HD runoff), but not carbonates. DIC concentrations were intermediate between clusters one and three (mean = 279 μM).

Cluster 3—Low DIC and SO_4^{2-}, High Dissolved Al^{3+}, and ^{13}C-Depleted CO_2

Bottles with active layer and Holocene sediments (except HC Holocene) had high concentrations of dissolved Al^{3+} (mean = 20.3 μM), consistently lower conductivity, moderate to low DIC (mean = 160 μM), low SO_4^{2-} (mean = 202 μM), and ^{13}C-depleted CO_2 (−16.3 to −20.3‰, n = 5) at 168 h (**Figure 3**, **Table 4**). There were no Pleistocene permafrost, runoff, or debris tongue sediments in this cluster.

DISCUSSION

Our findings reveal several interacting controls from thermokarst on fluvial inorganic carbon cycling on the Peel Plateau. In

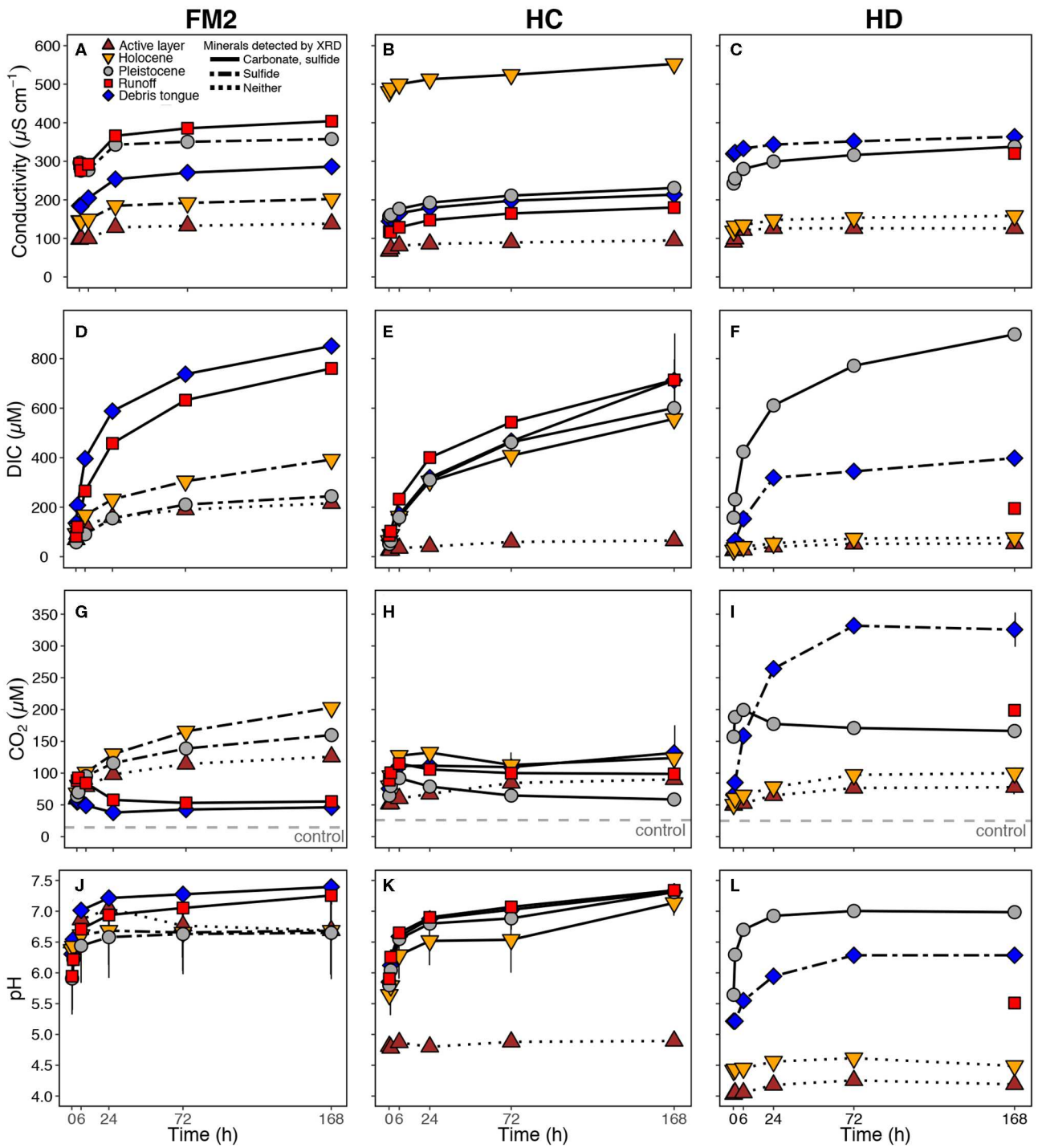

FIGURE 3 | Weathering experiment trends in **(A-C)** conductivity, **(D-F)** dissolved inorganic carbon (DIC), **(G-I)** dissolved CO2, and **(J-L)** pH by RTS and sediment source. Error bars represent ± standard deviation for conductivity, DIC, and CO_2, and range for pH (bars do not appear where smaller than symbol). See **Figure 1** for locations and **Table 1** for site characteristics. **(G–I)** Dashed lines represent CO_2 concentration in control bottles.

the modern and paleo (Holocene) active layer, we find that prior thaw and exposure of sediments to chemical weathering depleted carbonates, sulfides, and gypsum in these upper soil layers (Lacelle et al., 2019). In contrast, Pleistocene permafrost and recently thawed and colluviated sediments within the RTS runoff and debris tongue contain more of these readily

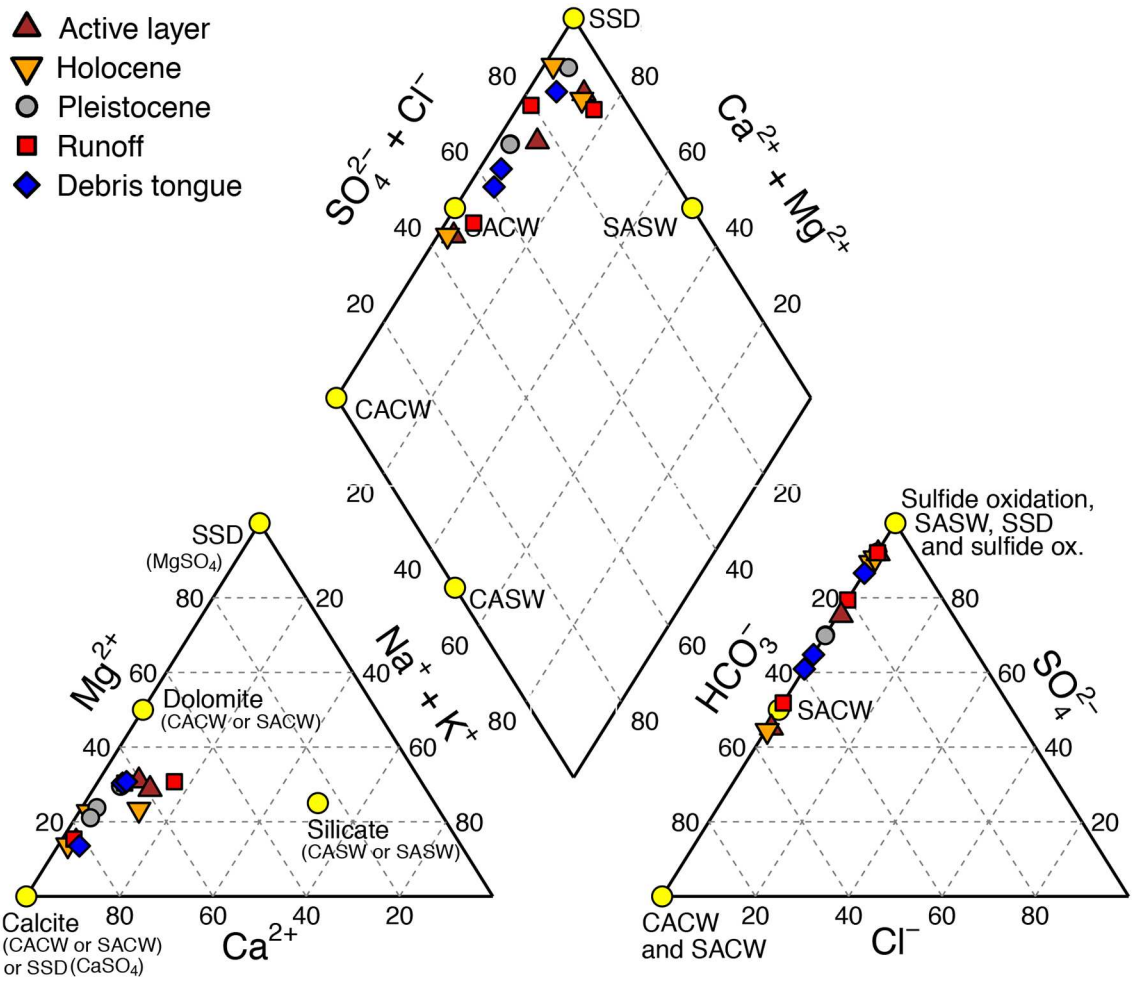

FIGURE 4 | Piper diagram showing the chemical composition of MilliQ water treated with five different retrogressive thaw slump sediments (see legend) exposed to varying degrees of prior thaw. The composition of each point reflects the relative concentrations (in meq L^{-1}) of major cations (left), anions (right), and both together (center) as a percent. See details in main text for calculation of end-members: CACW, H_2CO_3 carbonate weathering; SACW, H_2SO_4 carbonate weathering; CASW, H_2CO_3 silicate weathering; SASW, H_2SO_4 silicate weathering; SSD, sulfate salt (gypsum) dissolution.

weatherable sediments. Thus, thermokarst which unearths Pleistocene permafrost sediments at depth is more likely to intensify DIC cycling and abiotic CO_2 production by facilitating H_2SO_4 carbonate weathering, often in the presence of sulfides (Zolkos et al., 2018). Broadly, these trends show that renewed deglaciation on the Peel Plateau is accompanied by associated mineral weathering and biogeochemical dynamics documented in actively glacierized regions of the circumpolar north (Hindshaw et al., 2016; St. Pierre et al., 2019; Urra et al., 2019). These findings help to contextualize the effects of permafrost thaw on mineral weathering and inorganic carbon cycling on the Peel Plateau (**Figure 6**) and potentially in ice-rich, glaciated terrains elsewhere in northwestern Canada, Alaska, and Eurasia (Segal et al., 2016a; Kokelj et al., 2017a; Rudy et al., 2017).

Implications of Thaw History and Prior Sediment Exposure to Mineral Weathering for Inorganic Carbon Cycling

The lower conductivity observed in most treatments with active layer and Holocene sediments (except HC Holocene; **Table 2**, **Figure 5**) suggests that prior thaw of the upper layers of permafrost on the Peel Plateau promoted chemical weathering of readily-weathered minerals within the upper few meters of soil (Malone et al., 2013; Lacelle et al., 2019). Except for HC Holocene, active layer, and Holocene sediments did not have carbonate detected by XRD and also often had lower Ca/Sr and Ca/Na ratios. The relatively high DIC production associated with HC Holocene sediments may reflect the local presence of colluviated substrate from former debris flows that was integrated into permafrost during its upward aggradation

TABLE 4 | Measurements of water chemistry from the mineral weathering experiment at 168 h.

Site	Source	Cluster	pH	Cond ($\mu S\ cm^{-1}$)	DIC (μM)	Ca^{2+} (μM)	Mg^{2+} (μM)	Na^{+} (μM)	K^{+} (μM)	SO_4^{2-} (μM)	Cl^{-} (μM)	Al^{3+} (μM)	$\delta^{13}C_{CO_2}$ (‰ VPDB)
FM2	AL	3	6.69	138.2	215.9	642.2	114.4	13.9	38.6	90.3	3.4	7.9	−16.3
FM2	HO*	3	6.68	202.2	392.1	1009.8	165.0	10.9	37.1	157.5	2.3	8.7	−16.3
FM2	PL*	2	6.65	357.7	244.4	1093.6	496.2	79.6	103.6	1476.0	2.3	0.1	−7.8
FM2	RU**	1	7.25	404.2	760.4	1649.5	308.6	52.2	49.1	1471.1	2.5	0.2	−12.2
FM2	DT**	1	7.39	286.2	851.0	1152.0	190.5	61.3	67.8	783.4	1.4	0.3	−13.2
HC	AL	3	4.89	94.8	65.3	177.2	90.9	23.5	27.1	102.6	2.0	25.6	−20.2
HC	HO**	1	7.13	552.5	556.6	1974.6	594.1	30.4	72.1	2349.8	0.3	0.1	−8.3
HC	PL**	1	7.31	231.0	600.4	738.8	240.7	31.3	34.0	702.0	0.0	0.1	−9.6
HC	RU**	1	7.34	180.1	713.9	510.8	243.2	51.3	43.2	384.3	0.6	0.1	−11.1
HC	DT**	1	7.31	213.5	712.2	607.6	286.8	55.2	48.1	555.4	0.3	0.1	−12.5
HD	AL	3	4.19	126.1	53.1	169.4	82.3	34.4	35.3	313.6	2.5	10.0	−20.3
HD	HO	3	4.49	158.5	75.8	283.7	102.9	75.3	35.0	381.1	2.8	49.5	−19.1
HD	PL**	1	6.98	337.9	898.1	1212.4	337.4	36.1	67.0	1041.6	1.4	0.1	−9.9
HD	RU	2	5.51	320.4	195.0	725.1	421.3	349.7	99.0	1153.0	3.4	16.1	−6.9
HD	DT*	2	6.28	363.9	398.0	1047.7	509.8	126.6	76.0	1291.3	1.7	2.9	−4.7
Cluster means (standard error, range for pH)													
		1	7.2 (0.2)	315 (49)	728 (47)	1,121 (207)	314 (50)	45 (5)	54 (5)	1,041 (256)	0.9 (0.3)	0.1 (0)	−11.0 (0.7)
		2	5.9 (0.6)	347 (14)	279 (61)	955 (116)	476 (28)	185 (83)	93 (9)	1,307 (94)	2.4 (0.5)	6.4 (4.9)	−6.5 (0.9)
		3	4.7 (1.2)	144 (18)	160 (65)	456 (163)	111 (15)	32 (12)	35 (2)	209 (59)	2.6 (0.2)	20.3 (8)	−18.4 (0.9)
Source means (standard deviation, range for pH)													
	AL		4.6 (1.2)	120 (22)	111 (91)	330 (271)	96 (17)	24 (10)	34 (6)	169 (125)	2.6 (0.7)	14.5 (9.6)	−18.9 (2.3)
	HO		5.0 (1.3)	304 (216)	342 (244)	1,089 (848)	287 (268)	39 (33)	48 (21)	963 (1,206)	1.8 (1.3)	19.4 (26.4)	−14.6 (5.6)
	PL		6.9 (0.3)	309 (68)	581 (327)	1,015 (246)	358 (129)	49 (27)	68 (35)	1,073 (388)	1.2 (1.1)	0.1 (0)	−9.1 (1.1)
	RU		6.0 (0.9)	302 (113)	556 (314)	962 (605)	324 (90)	151 (172)	64 (31)	1,003 (559)	2.2 (1.4)	5.5 (9.2)	−10.1 (2.8)
	DT		6.7 (0.6)	288 (75)	654 (232)	936 (289)	329 (164)	81 (40)	64 (14)	877 (377)	1.1 (0.7)	1.1 (1.6)	−10.1 (4.7)

*AL, active layer; HO, Holocene; PL, Pleistocene; RU, runoff; DT, debris tongue. See text for details. Minerals detected by XRD: **Sulfides and carbonates, *sulfides.*

(Lacelle et al., 2019). The greater solute production associated with debris tongue sediments (**Figure 3**) indicates relatively limited weathering prior to burial within debris tongues, where some protection from wetting within the interior may reduce weathering prior to sample collection. Where RTSs on the Peel Plateau expose the Holocene active layer, the effects on fluvial inorganic carbon cycling will likely be greater if the substrate contains paleo debris flow material (Lacelle et al., 2019). The more modest DIC generation associated with active layer and Holocene sediments that did not contain debris tongue material suggests that carbonates were present, but in amounts typically minor enough to not be detected by XRD (here, <3%). This is consistent with observations of modern and paleo-active layer soils in Alaska (USA) and the central Yukon Territory (Canada), where top-down thaw promoted chemical weathering and a reduction of carbonates relative to silicates in upper soil layers (Burn et al., 1986; Keller et al., 2010). These findings broadly demonstrate that prior thaw and local and regional heterogeneity in soil composition are among the primary abiotic controls on fluvial inorganic carbon cycling on the Peel Plateau and likely in permafrost terrains across the circumpolar north.

Thermokarst Sediment Mineral Composition As a Driver of DIC Speciation in Streams

The grouping of treatments into distinct geochemical clusters indicates that thaw history enables a differentiation in mineralogy that provides an overarching control on the abiotic component of inorganic carbon cycling in thermokarst-affected streams on the Peel Plateau. Sediments in cluster one, which contained the most carbonates and sulfides (both >3%) and had more limited prior exposure to thaw, yielded the highest DIC concentrations and showed a trend of decreasing CO_2 after ∼24 h (**Figure 3**). The decrease in CO_2, high DIC, and elevated pH (mean = 7.2) associated with sediments in cluster one (**Figure 5**) suggests that H_2CO_3 carbonate weathering converted some of the initially-produced CO_2 to HCO_3^-. The decrease in $\delta^{13}C_{CO_2}$ values expected from this pH buffering (fractionation ca. −11‰) (Clark and Fritz, 1997) and the intermediate $\delta^{13}C_{CO_2}$ values for cluster one (−8 to −13‰) indicate weathering of carbonate sediments that were isotopically similar to regional bedrock ($\delta^{13}C$ carbonate = −0.7 to −5.6‰) (Hitchon and Krouse, 1972) that may be present within tills on the Peel Plateau. Together, these trends

for the cluster one treatments suggests that, when carbonates are sufficiently abundant, carbonate weathering by H_2CO_3 (Equation 2) and pH buffering (Equation 1) can fix some CO_2 as HCO_3^- (Brantley et al., 2014) and thereby partially offset the high rates of CO_2 production and efflux within RTSs on the Peel Plateau (Zolkos et al., 2019). Although we did not observe it in our treatments, sediments with abundant carbonate and limited or no sulfides would have even stronger CO_2 consumption (Striegl et al., 2007; St. Pierre et al., 2019). In contrast, the striking CO_2 production in treatments with a greater proportion of sulfide (cluster two) suggests that carbonate weathering was insufficient to noticeably temper dissolved CO_2 concentrations. Rather, more intense sulfide oxidation than carbonate weathering likely sustained a relatively low pH (mean = 5.9, **Table 2**) and enabled more complete dissolution of trace carbonates, resulting in $\delta^{13}C_{CO_2}$ (−6.5‰) reflective of an abiotic CO_2 source. In cluster three, the relatively more ^{13}C-depleted $\delta^{13}C_{CO_2}$ values (−16 to −20‰) may partly reflect the abiotic breakdown of organic matter from the modern and paleo Holocene active layer soils in a relatively acidic environment (Bao et al., 2019). For all clusters, concentrations of SO_4^{2-} were typically greater than would be expected from sulfide oxidation alone (section Mineral Weathering Experiment), indicating that gypsum dissolution generated a large proportion of the SO_4^{2-} that we observed in our experiment. This suggests that even a small proportion of SO_4^{2-} derived from sulfide oxidation can have critical implications for DIC cycling.

These findings build on recent work showing that RTSs exposing Pleistocene permafrost sediments can amplify inorganic carbon cycling (Zolkos et al., 2018) by revealing that the chemical weathering of these sediments on the Peel Plateau is most likely to be a net source of abiotic CO_2. This abiotic CO_2 flux from Peel Plateau thermokarst streams to the atmosphere—which occurs at high rates, but over a small area—is likely minor relative to CO_2 release from biotic processes occurring within recently thawed permafrost substrate (Littlefair and Tank, 2018; Zolkos et al., 2019) and from thickening of the active layer (Striegl et al., 2005). As thermokarst intensifies on the Peel Plateau, RTSs may increase fluvial export of HCO_3^- into marine environments, where climatic effects would unfold over geological timescales as carbonate precipitation reactions release CO_2 to the atmosphere (Calmels et al., 2007).

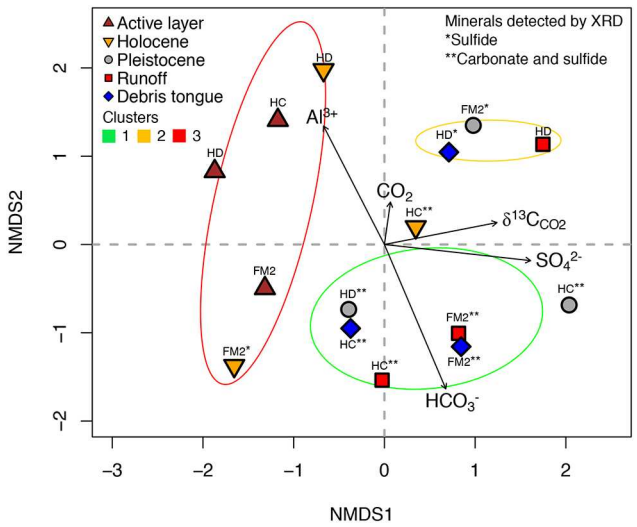

FIGURE 5 | *metaMDS* results showing similarities between measurements (proximate = more similar) and correlations between measurements and original observations (black text). Note RTS IDs included above measurements. Ellipses constrain statistical clusters in **Figure A1** (see section Results in main text).

Thermokarst Intensity As a Control on Inorganic Carbon Cycling on the Peel Plateau

These findings build on previous research showing that deeper RTSs on the Peel Plateau expose more solute-rich permafrost and are therefore likely to have a stronger effect on stream chemistry than shallow thermokarst (Kokelj et al., 2013; Malone et al., 2013; Lacelle et al., 2019). Here, we show that deeper RTSs also expose a greater proportion of previously unweathered carbonate- and sulfide-bearing Pleistocene permafrost sediments, and are thus likely to enhance inorganic carbon cycling upon thaw, resulting in greater DIC production (e.g., Zolkos et al., 2018). Further, the striking DIC production in treatments with runoff and debris

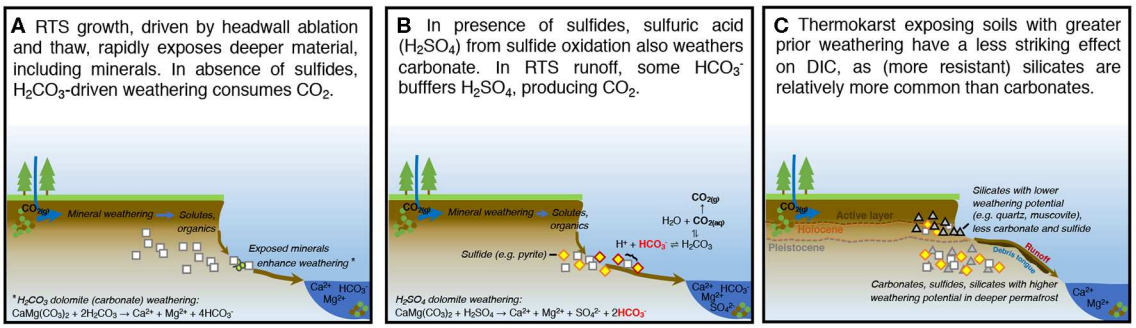

FIGURE 6 | Refined conceptual model of RTS effects on inorganic carbon cycling on the Peel Plateau **(A)** in the presence of carbonates and absence of sulfides and **(B)** in the presence of both carbonates and sulfides. **(C)** Depicts how this paper builds on previous understanding. Adapted from Zolkos et al. (2018).

tongue material reveals that these recently thawed sediments can augment fluvial inorganic carbon cycling for at least years to decades as RTSs develop. Initially, we reasoned that debris tongue sediments would have a limited effect on DIC, because this material is thawed and exposed at the surface environment prior to burial by subsequent debris flows (Kokelj et al., 2017b). Contrary to our hypothesis, RTS debris tongue sediments were associated with consistently strong DIC production, indicating greater protection from weathering and more limited depletion of carbonate and sulfide than the active layer and Holocene permafrost sediments. Mineral weathering in debris tongue environments may be enhanced as vegetation colonizes stabilized areas (Cray and Pollard, 2015) and as sediments erode into streams (van der Sluijs et al., 2018). From an inorganic carbon cycling perspective, this suggests that previously un-thawed sediments that are redistributed following thaw may be an important legacy of thermokarst on the Peel Plateau, particularly if increasing thaw and rainfall facilitate exposure and the transport of RTS sediments into stream networks (Kokelj et al., 2015; van der Sluijs et al., 2018). These interpretations align with observations of increasing downstream geochemical signals of carbonate weathering and sulfide oxidation (Zolkos et al., 2018) in conjunction with intensifying regional thermokarst in recent decades (Segal et al., 2016a). As future warming and increasing rainfall on the Peel Plateau increase RTS activity, the thawing of minerals in deeper permafrost can thus be expected to accelerate inorganic carbon cycling for decades to centuries.

Implications for the Role of Mineral Weathering Within Permafrost Carbon Feedbacks

Across the pan-Arctic, increasing riverine solute fluxes in recent decades signals a thickening of active layers, deepening flow paths, and enhanced mineral weathering in concert with climate warming and intensifying precipitation (Tank et al., 2016; Toohey et al., 2016; Drake et al., 2018a; Zolkos et al., 2018). While increasing riverine alkalinity fluxes in North America (Peel, Mackenzie; Tank et al., 2016; Zolkos et al., 2018) and Siberia (Ob', Yenisey; Drake et al., 2018a) reflect a broad scale acceleration of inorganic carbon cycling, stronger coupling between carbonate weathering and sulfide oxidation in northwestern Canada diminishes the weathering CO_2 sink compared to other Arctic regions (Beaulieu et al., 2012). From an Arctic carbon cycling perspective, regional variability in lithology, hydrology (Tank et al., 2012), and microbial processes (Hindshaw et al., 2016) influence the mineral weathering component of carbon-climate feedbacks. Recent work suggests that biotic processes drive DIC cycling in ice- and organic-rich (syngenetic) regions affected by thermokarst (Drake et al., 2018b). Working in a relatively more mineral-rich permafrost terrain, we show that intensifying thermokarst stands to amplify abiotic processes, but that the presence of sulfide oxidation is a primary control on the degree to which mineral weathering represents a CO_2 sink. Despite increasing recognition that mineral weathering is an important component of the northern carbon cycle (Calmels et al., 2007; Beaulieu et al., 2012; Tank et al., 2012, 2016), the contribution of thermokarst to these processes remains poorly constrained. This work indicates that thermokarst will have strong effects on inorganic carbon cycling where glaciated terrains coincide with carbonate lithologies (Zolkos et al., 2018; St. Pierre et al., 2019) and perhaps most strongly where sediments remain unmodified at the near surface (e.g., Rudy et al., 2017; Lewkowicz and Way, 2019; Ward Jones et al., 2019).

Thermokarst can expose large volumes of sediments to mineral weathering and fluvial transport (Kokelj et al., 2013; van der Sluijs et al., 2018), with unknown effects on CO_2 exchange between streams and the atmosphere as HCO_3^- is exported downstream. These effects are likely to be particularly strong across glacial deposits, where carbonates and sulfides are often highly reactive (Blum et al., 1998; Anderson et al., 2000; Torres et al., 2017) and even trace amounts can profoundly affect inorganic carbon cycling. Quantifying the fluvial CO_2: HCO_3^- balance across broader scales in thermokarst-affected fluvial networks will help to trace and better understand the effects of permafrost thaw on inorganic carbon cycling (Drake et al., 2018a).

CONCLUSIONS

In this study, we found evidence to suggest that thermokarst activity on the Peel Plateau will amplify inorganic carbon cycling where RTSs facilitate the exposure of deeper, previously unweathered permafrost sediments. Across the circumpolar north, future increases in inorganic carbon cycling will be strongest where thermokarst unearths carbonate-bearing tills with limited prior thaw and modification (Kokelj et al., 2017b). In these regions, the progression of—and balance between—H_2CO_3 and H_2SO_4 weathering will determine the degree to which DIC in freshwaters represents a CO_2 sink (Calmels et al., 2007; Tank et al., 2012, 2016; Drake et al., 2018a). By investigating the composition and reactivity of mineral substrate in permafrost regions elsewhere, particularly where thermokarst may expose and mobilize vast stores of minerals into fluvial networks (e.g., Olefeldt et al., 2016), future work will advance understanding of the role of mineral weathering within contemporary inorganic carbon cycling and long-term feedbacks within Earth's climate system (Schuur et al., 2015; Zolkos et al., 2018).

DATA AVAILABILITY STATEMENT

All datasets generated for this study are included in the article/ **Supplementary Material**.

AUTHOR CONTRIBUTIONS

SZ and ST designed the study. SZ led data analysis and interpretation and manuscript writing. ST contributed to data interpretation and manuscript writing.

FUNDING

Natural Sciences and Engineering Research Council of Canada supported research activities (Discovery Grant #430696, Northern Research Supplement #444873), Campus Alberta

Innovates Program supported laboratory research activities, Natural Resources Canada Polar Continental Shelf Program (#61717) supported field research activities. UAlberta Northern Research Award supported field research activities. Arctic Institute of North America Grant-in-Aid supported field research activities.

ACKNOWLEDGMENTS

We thank Rosemin Nathoo, Christine Firth, Abraham Snowshoe, Keith Collins, Sarah Shakil, Erin MacDonald, Dr. Lisa Bröder, and Kirsi Keskitalo for assistance in the field, and Yomna Elshamy for assistance in the laboratory. We thank Dr. Steve Kokelj and Dr. David Olefeldt for helpful comments on a draft of the manuscript. CAIP funding awarded to Dr. David Olefeldt supported the analyses of CO_2 stable isotopes. Data are provided within the manuscript and with the online version of the manuscript.

SUPPLEMENTARY MATERIAL

The Supplementary Material for this article can be found online at: https://www.frontiersin.org/articles/10.3389/feart.2020.00152/full#supplementary-material

Supplementary Material | The Supplementary Material for this study includes geochemistry data produced from the mineral weathering experiment.

REFERENCES

Anderson, S. P. (2007). Biogeochemistry of glacial landscape systems. *Annu. Rev. Earth Planet Sci.* 35, 375–399. doi: 10.1146/annurev.earth.35.031306.140033

Anderson, S. P., Drever, J. I., Frost, C. D., and Holden, P. (2000). Chemical weathering in the foreland of a retreating glacier. *Geochim. Cosmochim. Acta* 64, 1173–1189. doi: 10.1016/S0016-7037(99)00358-0

Bao, R., McNichol, A. P., Hemingway, J. D., Lardie Gaylord, M. C., and Eglinton, T. I. (2019). Influence of different acid treatments on the radiocarbon content spectrum of sedimentary organic matter determined by RPO/accelerator mass spectrometry. *Radiocarbon* 61, 395–413. doi: 10.1017/RDC.2018.125

Beaulieu, E., Goddéris, Y., Donnadieu, Y., Labat, D., and Roelandt, C. (2012). High sensitivity of the continental-weathering carbon dioxide sink to future climate change. *Nat. Clim. Change* 2, 346–349. doi: 10.1038/nclimate1419

Berner, R. A. (1999). A new look at the long-term carbon cycle. *GSA Today* 9, 1–6.

Biskaborn, B. K., Smith, S. L., Noetzli, J., Matthes, H., Vieira, G., Streletskiy, D. A., et al. (2019). Permafrost is warming at a global scale. *Nat. Commun.* 10:264. doi: 10.1038/s41467-018-08240-4

Blum, J. D., Gazis, C. A., Jacobson, A. D., and Chamberlain, C. P. (1998). Carbonate versus silicate weathering in the Raikhot watershed within the high himalayan crystalline series. *Geology* 26, 411–414. doi: 10.1130/0091-7613(1998)026<0411:CVSWIT>2.3.CO;2

Brantley, S. L., Lebedeva, M., and Bazilevskaya, E. (2014). "Relating weathering fronts for acid neutralization and oxidation to pCO_2 and pO_2," in *Treatise on Geochemistry* (Elsevier), 327–352. Available online at: https://linkinghub.elsevier.com/retrieve/pii/B9780080959757013176 (accessed July 3, 2019).

Burn, C. R. (1997). Cryostratigraphy, paleogeography, and climate change during the early holocene warm interval, western Arctic coast, Canada. *Can. J. Earth Sci.* 34, 912–925. doi: 10.1139/e17-076

Burn, C. R., Michel, F. A., and Smith, M. W. (1986). Stratigraphic, isotopic, and mineralogical evidence for an early Holocene thaw unconformity at mayo, yukon territory. *Can. J. Earth Sci.* 23, 794–803. doi: 10.1139/e86-081

Calmels, D., Gaillardet, J., Brenot, A., and France-Lanord, C. (2007). Sustained sulfide oxidation by physical erosion processes in the mackenzie river basin: climatic perspectives. *Geology* 35, 1003–1006. doi: 10.1130/G24132A.1

Clark, I. D., and Fritz, P. (1997). *Environmental Isotopes in Hydrogeology.* Boca Raton, FL: CRC Press/Lewis Publishers.

Cooper, H. K., Duke, M. J. M., Simonetti, A., and Chen, G. (2008). Trace element and Pb isotope provenance analyses of native copper in northwestern North America: results of a recent pilot study using INAA, ICP-MS, and LA-MC-ICP-MS. *J. Archaeol. Sci.* 35, 1732–1747. doi: 10.1016/j.jas.2007.11.012

Cray, H. A., and Pollard, W. H. (2015). Vegetation recovery patterns following permafrost disturbance in a low arctic setting: case study of herschel Island, Yukon, Canada. *Arct. Antarct. Alp. Res.* 47, 99–113. doi: 10.1657/AAAR0013-076

Drake, T. W., Guillemette, F., Hemingway, J. D., Chanton, J. P., Podgorski, D. C., Zimov, N. S., et al. (2018a). The ephemeral signature of permafrost carbon in an arctic fluvial network. *J. Geophys. Res. Biogeosciences*. 123, 1–11. doi: 10.1029/2017JG004311

Drake, T. W., Tank, S. E., Zhulidov, A. V., Holmes, R. M., Gurtovaya, T., and Spencer, R. G. M. (2018b). Increasing alkalinity export from large russian arctic rivers. *Environ. Sci. Technol.* 52, 8302–8308. doi: 10.1021/acs.est.8b01051

Duk-Rodkin, A., and Hughes, O. L. (1992). Surficial geology, fort McPherson-bell river, yukon-Northwest territories. *Geol. Surv. Can.* doi: 10.4095/184002

Fritz, M., Wetterich, S., Schirrmeister, L., Meyer, H., Lantuit, H., Preusser, F., et al. (2012). Eastern beringia and beyond: late wisconsinan and holocene landscape dynamics along the Yukon Coastal Plain, Canada. *Palaeogeogr. Palaeoclimatol. Palaeoecol.* 319–320, 28–45. doi: 10.1016/j.palaeo.2011.12.015

Gaillardet, J., Dupré, B., Louvat, P., and Allegre, C. J. (1999). Global silicate weathering and CO_2 consumption rates deduced from the chemistry of large rivers. *Chem. Geol.* 159, 3–30. doi: 10.1016/S0009-2541(99)00031-5

Gislason, S. R., Oelkers, E. H., Eiriksdottir, E. S., Kardjilov, M. I., Gisladottir, G., Sigfusson, B., et al. (2009). Direct evidence of the feedback between climate and weathering. *Earth Planet. Sci. Lett.* 277, 213–222. doi: 10.1016/j.epsl.2008.10.018

Hesslein, R. H., Rudd, J. W. M., Kelly, C., Ramlal, P., and Hallard, K. A. (1991). "Carbon dioxide pressure in surface waters of Canadian lakes," in *Air-Water Mass Transfer: Selected Papers From the Second International Symposium on Gas Transfer at Water Surfaces*, eds S. C. Wilhelms and J. S. Gulliver (New York, NY: American Society of Civil Engineers), 413–431.

Hindshaw, R. S., Heaton, T. H. E., Boyd, E. S., Lindsay, M. R., and Tipper, E. T. (2016). Influence of glaciation on mechanisms of mineral weathering in two high Arctic catchments. *Chem. Geol.* 420, 37–50. doi: 10.1016/j.chemgeo.2015.11.004

Hitchon, B., and Krouse, H. R. (1972). Hydrogeochemistry of the surface waters of the mackenzie river drainage basin, Canada-III. Stable isotopes of oxygen, carbon and sulphur. *Geochim. Cosmochim. Acta* 36, 1337–1357. doi: 10.1016/0016-7037(72)90066-X

Keller, K., Blum, J. D., and Kling, G. W. (2007). Geochemistry of soils and streams on surfaces of varying ages in arctic alaska. *Arct. Antarct. Alp. Res.* 39, 84–98. doi: 10.1657/1523-0430(2007)39[84:GOSASO]2.0.CO;2

Keller, K., Blum, J. D., and Kling, G. W. (2010). Stream geochemistry as an indicator of increasing permafrost thaw depth in an arctic watershed. *Chem. Geol.* 273, 76–81. doi: 10.1016/j.chemgeo.2010.02.013

Kokelj, S. V., Lacelle, D., Lantz, T. C., Tunnicliffe, J., Malone, L., Clark, I. D., et al. (2013). Thawing of massive ground ice in mega slumps drives increases in stream sediment and solute flux across a range of watershed scales. *J. Geophys. Res. Earth Surf.* 118, 681–692. doi: 10.1002/jgrf.20063

Kokelj, S. V., Lantz, T. C., Tunnicliffe, J., Segal, R., and Lacelle, R. (2017a). Climate-driven thaw of permafrost preserved glacial landscapes, northwestern Canada. *Geology* 45, 371–374. doi: 10.1130/G38626.1

Kokelj, S. V., Tunnicliffe, J., Lacelle, D., Lantz, T. C., Chin, K. S., and Fraser, R. (2015). Increased precipitation drives mega slump development and destabilization of ice-rich permafrost terrain, northwestern Canada. *Glob. Planet. Change* 129, 56–68. doi: 10.1016/j.gloplacha.2015.02.008

Kokelj, S. V., Tunnicliffe, J. F., and Lacelle, D. (2017b). "The peel plateau of northwestern canada: an ice-rich hummocky moraine landscape in transition,"

in *Landscapes and Landforms of Western Canada*, ed O. Slaymaker (Cham: Springer International Publishing) 109–122. Available online at: http://link.springer.com/10.1007/978-3-319-44595-3_7 (accessed September 21, 2017).

Lacelle, D. (2004). Segregated-intrusive ice of subglacial meltwater origin in retrogressive thaw flow headwalls, Richardson Mountains, NWT, Canada. *Quat. Sci. Rev.* 23, 681–696. doi: 10.1016/j.quascirev.2003.09.005

Lacelle, D., Brooker, A., Fraser, R. H., and Kokelj, S. V. (2015). Distribution and growth of thaw slumps in the Richardson Mountains–Peel Plateau region, northwestern Canada. *Geomorphology* 235, 40–51. doi: 10.1016/j.geomorph.2015.01.024

Lacelle, D., Fontaine, M., Pellerin, A., Kokelj, S. V., and Clark, I. D. (2019). Legacy of holocene landscape changes on soil biogeochemistry: a perspective from paleo-active layers in northwestern Canada. *J. Geophys. Res. Biogeosci.* 2018:JG004916. doi: 10.1029/2018JG004916

Lacelle, D., Lauriol, B., Zazula, G., Ghaleb, B., Utting, N., and Clark, I. D. (2013). Timing of advance and basal condition of the Laurentide Ice Sheet during the last glacial maximum in the Richardson Mountains, NWT. *Quat. Res.* 80, 274–283. doi: 10.1016/j.yqres.2013.06.001

Lehn, G. O., Jacobson, A. D., Douglas, T. A., McClelland, J. W., Barker, A. J., and Khosh, M. S. (2017). Constraining seasonal active layer dynamics and chemical weathering reactions occurring in North Slope Alaskan watersheds with major ion and isotope ($\delta^{34}S_{SO4}$, $\delta^{13}C_{DIC}$, $^{87}Sr/^{86}Sr$, $\delta^{44/40}Ca$, and $\delta^{44/42}Ca$) measurements. *Geochim. Cosmochim. Acta* 217, 399–420. doi: 10.1016/j.gca.2017.07.042

Lerman, A., Wu, L., and Mackenzie, F. T. (2007). CO_2 and H_2SO_4 consumption in weathering and material transport to the ocean, and their role in the global carbon balance. *Mar. Chem.* 106, 326–350. doi: 10.1016/j.marchem.2006.04.004

Lewkowicz, A. G., and Way, R. G. (2019). Extremes of summer climate trigger thousands of thermokarst landslides in a High Arctic environment. *Nat. Commun.* 10:1329. doi: 10.1038/s41467-019-09314-7

Li, M., Peng, C., Wang, M., Xue, W., Zhang, K., Wang, K., et al. (2017). The carbon flux of global rivers: a re-evaluation of amount and spatial patterns. *Ecol. Indic.* 80, 40–51. doi: 10.1016/j.ecolind.2017.04.049

Littlefair, C. A., and Tank, S. E. (2018). Biodegradability of thermokarst carbon in a till-associated, glacial margin landscape: the case of the peel plateau, NWT, Canada. *J. Geophys. Res. Biogeosci.* 123, 3293–3307. doi: 10.1029/2018JG004461

Littlefair, C. A., Tank, S. E., and Kokelj, S. V. (2017). Retrogressive thaw slumps temper dissolved organic carbon delivery to streams of the Peel Plateau, NWT, Canada. *Biogeosciences* 14, 5487–5505. doi: 10.5194/bg-14-5487-2017

Maher, K., and Chamberlain, C. P. (2014). Hydrologic regulation of chemical weathering and the geologic carbon cycle. *Science* 343, 1502–1504. doi: 10.1126/science.1250770

Malone, L., Lacelle, D., Kokelj, S., and Clark, I. D. (2013). Impacts of hillslope thaw slumps on the geochemistry of permafrost catchments (Stony Creek watershed, NWT, Canada). *Chem. Geol.* 356, 38–49. doi: 10.1016/j.chemgeo.2013.07.010

Mandile, A. J., and Hutton, A. C. (1995). Quantitative X-ray diffraction analysis of mineral and organic phases in organic-rich rocks. *Int. J. Coal Geol.* 28, 51–69. doi: 10.1016/0166-5162(95)00004-W

Michel, F. A. (2011). Isotope characterisation of ground ice in northern Canada. *Permafr. Periglac. Process.* 22, 3–12. doi: 10.1002/ppp.721

Montross, S. N., Skidmore, M., Tranter, M., Kivimäki, A.-L., and Parkes, R. J. (2013). A microbial driver of chemical weathering in glaciated systems. *Geology* 41, 215–218. doi: 10.1130/G33572.1

Norris, D. K. (1985). *Geology of the Northern Yukon and Northwestern District of Mackenzie,* Map 1581A, scale: 1:500,000. Ottawa, ON: Geological Survey of Canada. doi: 10.4095/120537

Oksanen, J., Blanchet, F. G., Kindt, R., Legendre, P., Minchin, P. R., O'Hara, R., et al. (2013). *Package 'Vegan'. Community Ecology Package, Version 2.4-6.* Available online at: http://CRAN.R-project.org/package=vegan

Olefeldt, D., Goswami, S., Grosse, G., Hayes, D., Hugelius, G., Kuhry, P., et al. (2016). Circumpolar distribution and carbon storage of thermokarst landscapes. *Nat. Commun.* 7:13043. doi: 10.1038/ncomms13043

Pierrot, D., Lewis, E., and Wallace, D. W. R. (2006). *MS Excel Program Developed for CO_2 System Calculations*. Available online at: doi: 10.3334/CDIAC/otg. CO2SYS_XLS_CDIAC105a

Piper, A. M. (1944). A graphic procedure in the geochemical interpretation of water-analyses. *Trans. Am. Geophys. Union* 25:914. doi: 10.1029/TR025i006p00914

Pogge von Strandmann, P. A. E., Desrochers, A., Murphy, M. J., Finlay, A. J., Selby, D., and Lenton, T. M. (2017). Global climate stabilisation by chemical weathering during the Hirnantian glaciation. *Geochem. Perspect. Lett.* 3, 230–237. doi: 10.7185/geochemlet 1726

R Core Team (2018). *R: A Language and Environment for Statistical Computing*. Vienna: R Foundation for Statistical Computing. Available online at: http://www.r-project.org/

Riebe, C. S., Kirchner, J. W., Granger, D. E., and Finkel, R. C. (2001). Strong tectonic and weak climatic control of long-term chemical weathering rates. *Geology* 29, 511–514. doi: 10.1130/0091-7613(2001)029<0511:STAWCC>2.0.CO;2

Rimstidt, J. D., and Vaughan, D. J. (2003). Pyrite oxidation: a state-of-the-art assessment of the reaction mechanism. *Geochim. Cosmochim. Acta* 67, 873–880. doi: 10.1016/S0016-7037(02)01165-1

Rudy, A. C. A., Lamoureux, S. F., Kokelj, S. V., Smith, I. R., and England, J. H. (2017). Accelerating thermokarst transforms ice-cored terrain triggering a downstream cascade to the ocean. *Geophys. Res. Lett.* 44, 11080–11087. doi: 10.1002/2017GL074912

Schuur, E. A. G., McGuire, A. D., Schädel, C., Grosse, G., Harden, J. W., Hayes, D. J., et al. (2015). Climate change and the permafrost carbon feedback. *Nature* 520, 171–179. doi: 10.1038/nature14338

Segal, R. A., Lantz, T. C., and Kokelj, S. V. (2016a). Acceleration of thaw slump activity in glaciated landscapes of the Western Canadian Arctic. *Environ. Res. Lett.* 11:034025. doi: 10.1088/1748-9326/11/3/034025

Segal, R. A., Lantz, T. C., and Kokelj, S. V. (2016b). *Inventory of active retrogressive thaw slumps in the Peel Plateau, Northwest Territories, Northwest Territories Geological Survey*. NWT Open Report 2015-020. Yellowknife, NT: Northwest Territories Geological Survey, p. 7.

Serreze, M. C., and Barry, R. G. (2011). Processes and impacts of arctic amplification: a research synthesis. *Glob. Planet. Change* 77, 85–96. doi: 10.1016/j.gloplacha.2011.03.004

Singer, P. C., and Stumm, W. (1970). Acidic mine drainage: the rate-determining step. *Science* 167, 1121–1123. doi: 10.1126/science.167.3921.1121

Skidmore, M., Sharp, M., and Tranter, M. (2004). Kinetic isotopic fractionation during carbonate dissolution in laboratory experiments: Implications for detection of microbial CO_2 signatures using δ^{13}C-DIC. *Geochim. Cosmochim. Acta* 68, 4309–4317. doi: 10.1016/j.gca.2003.09.024

Stott, D. F. (1991). "Geotectonic correlation chart, sheet 1, Northwest territories and yukon," in *Sedimentary Cover of the Craton in Canada*, eds D. F. Stott and J. D. Aiken (Ottawa, ON: Geological Survey of Canada).

St. Pierre, K. A., St. Louis, V. L., Schiff, S. L., Lehnherr, I., Dainard, P. G., Gardner, A. S., et al. (2019). Proglacial freshwaters are significant and previously unrecognized sinks of atmospheric CO_2. *Proc. Natl. Acad. Sci. U.S.A.* 3:17690–17695. doi: 10.1073/pnas.1904241116

Striegl, R. G., Aiken, G. R., Dornblaser, M. M., Raymond, P. A., and Wickland, K. P. (2005). A decrease in discharge-normalized DOC export by the Yukon River during summer through autumn. *Geophys. Res. Lett.* 32, 1–4. doi: 10.1029/2005GL024413

Striegl, R. G., Dornblaser, M. M., Aiken, G. R., Wickland, K. P., and Raymond, P. A. (2007). Carbon export and cycling by the Yukon, Tanana, and Porcupine rivers, Alaska, 2001-2005. *Water Resour. Res.* 43:W02411. doi: 10.1029/2006WR005201

Stumm, W., and Morgan, J. J. (1996). *Aquatic Chemistry: Chemical Equilibria and Rates in Natural Waters, 3rd Edn.* NY: John Wiley & Son, Inc.

Suzuki, R., and Shimodaira, H. (2015). *pvclust: Hierarchical Clustering with P-Values via Multiscale Bootstrap Resampling, Version 2.0-0.* Available online at: https://cran.r-project.org/web/packages/pvclust/index.html

Tank, S. E., Raymond, P. A., Striegl, R. G., McClelland, J. W., Holmes, R. M., Fiske, G. J., et al. (2012). A land-to-ocean perspective on the magnitude, source and implication of DIC flux from major Arctic rivers to the Arctic Ocean. *Glob. Biogeochem. Cycles* 26, 1–15. doi: 10.1029/2011GB004192

Tank, S. E., Striegl, R. G., McClelland, J. W., and Kokelj, S. V. (2016). Multi-decadal increases in dissolved organic carbon and alkalinity flux from the Mackenzie drainage basin to the Arctic Ocean. *Environ. Res. Lett.* 11:054015. doi: 10.1088/1748-9326/11/5/054015

Toohey, R. C., Herman-Mercer, N. M., Schuster, P. F., Mutter, E. A., and Koch, J. C. (2016). Multidecadal increases in the Yukon River Basin of chemical fluxes as

indicators of changing flowpaths, groundwater, and permafrost. *Geophys. Res. Lett.* 43, 12120–12130. doi: 10.1002/2016GL070817

Torres, M. A., Moosdorf, N., Hartmann, J., Adkins, J. F., and West, A. J. (2017). Glacial weathering, sulfide oxidation, and global carbon cycle feedbacks. *Proc. Natl. Acad. Sci. U.S.A.* 114, 8716–8721. doi: 10.1073/pnas.1702953114

Torres, M. A., West, A. J., and Li, G. (2014). Sulphide oxidation and carbonate dissolution as a source of CO_2 over geological timescales. *Nature* 507, 346–349. doi: 10.1038/nature13030

Tranter, M., and Wadham, J. L. (2014). "Geochemical weathering in glacial and proglacial environments," in *Treatise on Geochemistry* (Elsevier), 157–173. Available online at: http://linkinghub.elsevier.com/retrieve/pii/B9780080959757005052 (accessed September 21, 2017).

Turetsky, M. R., Abbott, B. W., Jones, M. C., Walter Anthony, K., Olefeldt, D., Schuur, E. A. G., et al. (2020). Carbon release through abrupt permafrost thaw. *Nat. Geosci*. 13, 138–143. doi: 10.1038/s41561-019-0526-0

Urra, A., Wadham, J., Hawkings, J. R., Telling, J., Hatton, J. E., Yde, J. C., et al. (2019). Weathering dynamics under contrasting greenland ice sheet catchments. *Front. Earth Sci.* 7:299. doi: 10.3389/feart.2019.00299

van der Sluijs, J., Kokelj, S. V., Fraser, R. H., Tunnicliffe, J., and Lacelle, D. (2018). Permafrost terrain dynamics and infrastructure impacts revealed by UAV photogrammetry and thermal imaging. *Remote Sens.* 30:1734. doi: 10.3390/rs10111734

Vonk, J. E., Tank, S. E., and Walvoord, M. A. (2019). Integrating hydrology and biogeochemistry across frozen landscapes. *Nat. Commun.* 10:5377. doi: 10.1038/s41467-019-13361-5

Ward Jones, M. K., Pollard, W. H., and Jones, B. M. (2019). Rapid initialization of retrogressive thaw slumps in the Canadian high Arctic and their response to climate and terrain factors. *Environ. Res. Lett.* 14, 1–14. doi: 10.1088/1748-9326/ab12fd

Weiss, R. F. (1974). Carbon dioxide in water and seawater: the solubility of a non-ideal gas. *Mar. Chem.* 2, 203–215. doi: 10.1016/0304-4203(74)90015-2

West, A., Galy, A., and Bickle, M. (2005). Tectonic and climatic controls on silicate weathering. *Earth Planet. Sci. Lett.* 235, 211–228. doi: 10.1016/j.epsl.2005.03.020

Wolf, D. C., and Skipper, H. D. (1994). "Soil sterilization," in *Methods of Soil Analysis: Part 2—Microbiological and Biochemical Properties*, eds R. W. Weaver, S. Angle, P. Bottomley, D. Bezdicek, S. Smith, A. Tabatabai, and A. Wollum (Madison, WI: Soil Science Society of America) 41–51.

Zolkos, S., and Tank, S. E. (2019). Permafrost geochemistry and retrogressive thaw slump morphology (Peel Plateau, Canada), v. 1.0 (2017-2017). *Nord. D.* doi: 10.5885/45573XD-28DD57D553F14BF0

Zolkos, S., Tank, S. E., and Kokelj, S. V. (2018). Mineral weathering and the permafrost carbon-climate feedback. *Geophys. Res. Lett.* 45, 9623–9632. doi: 10.1029/2018GL078748

Zolkos, S., Tank, S. E., Striegl, R. G., and Kokelj, S. V. (2019). Thermokarst effects on carbon dioxide and methane fluxes in streams on the peel plateau (NWT, Canada). *J. Geophys. Res. Biogeosci.* 2019:JG005038. doi: 10.1029/2019JG005038

Zuberer, D. A. (1994). "Recovery and enumeration of viable bacteria," in *Methods of Soil Analysis: Part 2—Microbiological and Biochemical Properties*, eds R. W. Weaver, S. Angle, P. Bottomley, D. Bezdicek, S. Smith, A. Tabatabai, and A. Wollum (Madison, WI: Soil Science Society of America) 119–144.

Conflict of Interest: The authors declare that the research was conducted in the absence of any commercial or financial relationships that could be construed as a potential conflict of interest.

APPENDIX

TABLE A1 | The chemical composition of MilliQ de-ionized water in the control bottles at 168 h.

Site	Conductivity ($\mu S\ cm^{-1}$)	DIC (μM)	CO_2 (μM)	SO_4^{2-} (μM)	Cl^- (μM)	Ca^{2+} (μM)	Mg^{2+} (μM)	Na^+ (μM)	K^+ (μM)	Fe (μM)	Al^{3+} (μM)
FM2	1.9 ± 0.6	23.4 ± 0.2	14.5 ± 1.3	bd	bd	0.8	0.4	13.1	0.3	bd	0.1
HC	1.5 ± 0.4	26.8 ± 2.2	26.0	bd	1.1	bd	bd	bd	bd	bd	bd
HD	1.6 ± 0.6	25.1 ± 2.4	24.9 ± 1.0	bd	bd	bd	bd	bd	bd	bd	bd

Conductivity, dissolved inorganic carbon (DIC), and CO_2 are reported as mean of replicates ± standard deviation. bd, below detection.

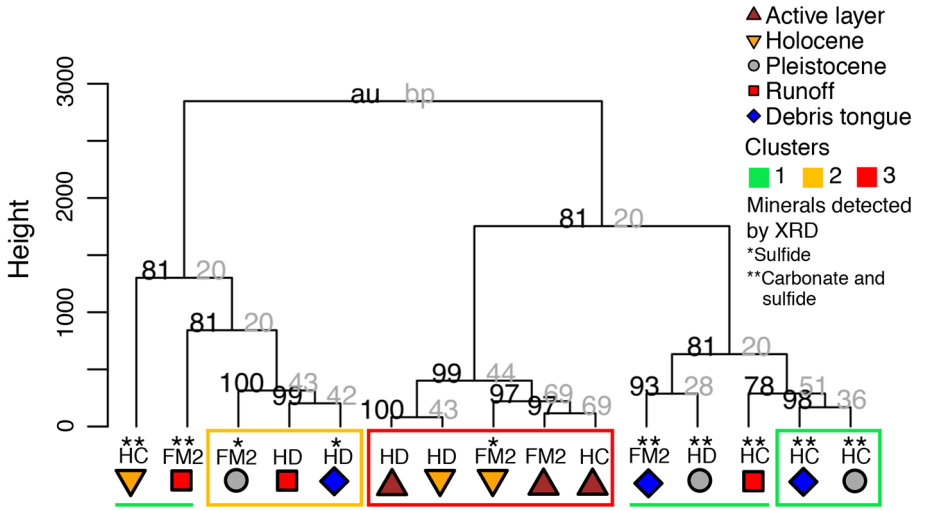

FIGURE A1 | Geochemical clusters from the *pvclust* analysis. Rectangles denote clusters where $p < 0.05$. au, approximately unbiased *p*-value; bp, bootstrapped probability.